Bone Reports 19 (2023) 101726

Contents lists available at ScienceDirect

Bone Reports

journal homepage: www.elsevier.com/locate/bonr

Novel approaches to correlate computerized tomography imaging of bone fracture callus to callus structural mechanics

Yazan Kadkoy [a,b], Sangeeta Abraham [a,b,1], Peter Michael [c], Tasmima Tazin [a], Charlene Wetterstrand [a], J. Patrick O'Connor [a,b,*]

[a] Department of Orthopaedics, Rutgers-New Jersey Medical School, Newark, United States of America
[b] Rutgers Biomedical Health Sciences, School of Graduate Studies, Newark, United States of America
[c] Department of Biomedical Engineering, New Jersey Institute of Technology, United States of America

ARTICLE INFO

Keywords:
Fracture callus
Bone
Micro-computed tomography
Mechanical strength
Z-ray

ABSTRACT

Estimating the mechanical properties of bone in vivo without destructive testing would be useful for research and clinical orthopedic applications. Micro-computerized tomography (μCT) imaging can provide quantitative, high-resolution 3D representations of bone morphology and is generally the basis from which bone mechanical properties are non-destructively estimated. The goal of this study was to develop metrics using qualitative and quantitative aspects of bone microarchitecture derived from μCT imaging to estimate the mechanical integrity of bone fracture calluses. Mechanical testing data (peak torque) and μCT image data from 12 rat femur fractures were collected at 4 weeks after fracture. MATLAB was used to analyze the callus μCT imaging data which were then correlated to the empirically determined peak torque of the callus. One metric correlated *Z*-rays, linear contiguities of voxels running parallel to the neutral axis of the femur and through the fracture callus, to peak torque. Other metrics were based on voxel linkage values (LVs), which is a novel measurement defined by the number of voxels surrounding a given voxel (ranging from 1 to 27) that are all above a specified threshold. Linkage values were utilized to segment the callus and compute healing scores (termed eRUST) based on the modified Radiographic Union Score for Tibial fractures (mRUST). Linkage values were also used to calculate linked bone areas (LBAs). All metrics positively correlated with peak torque, yielding correlations of determination (R^2) of 0.863 for eRUST, 0.792 for *Z*-ray scoring, and 0.764 for a normalized Linked Bone Area metric. These novel metrics appear to be promising approaches for extrapolating fracture callus structural properties from bone microarchitecture using objective analytical methods and without resorting to computationally complex finite element analyses.

1. Introduction

There are no objective standards for determining the progress of fracture healing in clinical settings. Bone fractures heal by tissue regeneration and are generally treated by aligning and juxtaposing the fractured bone ends (reduction) and mechanically stabilizing the fractured bone (fixation) to help ensure consolidation of the fractured bone, restoration of mechanical integrity, and restoration of anatomy. Healing is considered complete when the patient has regained normal, pain-free use of the affected bone. In many cases, healing is aided by limited use of the affected bone during the regenerative process (Kenwright et al., 1986; Augat et al., 1996; Anani and Castillo, 2022). However, there is no objective assessment to guide physicians as to when a bone has healed sufficiently for patients to begin physical rehabilitation, such as limited weightbearing, in order to bolster healing (Wittauer et al., 2021). Furthermore, there are no standard criteria to gauge when a fractured bone has regenerated sufficiently to countenance unrestricted use of the affected bone nor to discriminate between a healing complication that involves the bone as opposed to nerve or other soft-tissue complications that may prevent normal, pain-free use of the affected bone (Morshed

* Corresponding author at: Rutgers-New Jersey Medical, Dept. of Orthopaedics, Medical Sciences Building, Room E-659, 185 South Orange Ave., Newark, NJ 07103, United States of America.
E-mail addresses: yk399@njms.rutgers.edu (Y. Kadkoy), sabraham@exponent.com (S. Abraham), peter.a.michael@njit.edu (P. Michael), tt337@njms.rutgers.edu (T. Tazin), cew147@njms.rutgers.edu (C. Wetterstrand), oconnojp@njms.rutgers.edu (J.P. O'Connor).
[1] Current address: Exponent, 1250 S Capital of Texas Hwy., Bldg 3, Ste. 400, Austin, TX 78746.

https://doi.org/10.1016/j.bonr.2023.101726
Received 23 June 2023; Received in revised form 15 September 2023; Accepted 12 November 2023
Available online 13 November 2023
2352-1872/© 2023 The Authors. Published by Elsevier Inc. This is an open access article under the CC BY-NC-ND license (http://creativecommons.org/licenses/by-nc-nd/4.0/).

et al., 2008).

Re-establishing the mechanical integrity of a fractured bone is a critical parameter for successful fracture healing. In research studies, samples collected from experimental animals can be measured directly to determine the mechanical integrity of the healing bone, usually by destructive mechanical testing (Turner and Burr, 1993). However, in clinical practice or for longitudinally assessing healing in an animal subject, indirect, non-destructive techniques must be employed to assess healing progression and completion.

The most common method to diagnose a fracture, assess healing, or examine bone structure is radiographic (X-ray) imaging (Cunningham et al., 2017). Correlations exist between radiographic characteristics of a fracture callus and the mechanical integrity of the callus (Willems et al., 2022). However, those radiographic characteristics do not explain all the variance observed between callus radiological features and measured callus mechanical integrity (Willems et al., 2022). For example, use of radiography to assess fracture callus stiffness was found to have a sensitivity of 62 % and a specificity of 77 % in terms of diagnostic accuracy (Yang et al., 2013). Similarly, clinical evaluation and the ability of patients to tolerate use of or bear weight on the affected bone can also be highly subjective (Ruiz et al., 2014). These ambiguities make determining the stage to which fracture healing has progressed and when patients can initiate normal activity difficult.

Computed tomography (CT) and micro-computed tomography (μCT) are effective and non-destructive radiographic imaging methods to visualize and measure the external and internal structure of fracture calluses, bone, and other tissues in three dimensions (3D) (Morgan et al., 2009). Common bone structural features measured using μCT imaging include bone volume (BV), tissue volume (TV), bone volume fraction (BV/TV), bone trabecular thickness (Tb.Th), and trabecular spacing (Tb.Sp), among others (Bouxsein et al., 2010). Some bone architectural measurements derived from μCT imaging have been correlated to the mechanical properties of intact bone and of fracture calluses (Morgan et al., 2009; Nyman et al., 2009; Willems et al., 2022). However, the reported correlations between μCT parameters and mechanical properties are not high and, as with radiographic criteria, often fail to explain the variation seen in mechanical testing data (Willems et al., 2022). Finite element analysis (FEA) using μCT imaging data can better predict bone mechanical properties, but is model dependent, time-consuming, computationally intensive, and requires substantial expertise (Shefelbine et al., 2005; Weis et al., 2012).

Our goal is to establish an indirect measure of fracture callus mechanical integrity using μCT image data from which fracture callus mechanical properties and fracture healing progression can be objectively estimated. Here, we tested correlations between alternative evaluations of fracture callus μCT image data to empirically measured callus mechanical properties. μCT and mechanical testing data from fractured rat femurs collected at 28 days after fracture were used. The μCT data were analyzed using custom MATLAB scripts in which standard (grayscale) and a novel measure of μCT voxel quality, termed linkage value (LV), were used to calculate measures of bone healing. The metrics calculated using linkage values were correlated to the mechanical properties and to standardized radiographic scores (mRUST) of the fractured femurs. We found that the novel μCT metrics of number of longest *Z*-rays, normalized minimum Linked Bone Area, and a computed healing score (eRUST) correlated well with callus mechanical peak torque ($R^2 = 0.79$, 0.76, and 0.86, respectively).

2. Materials and methods

2.1. μCT image data

μCT image and mechanical testing data were obtained from a previous study examining femur fracture healing in male Sprague-Dawley rats (Table 1) (Subramanian, 2015). The fracture healing experiment was approved by the Rutgers-New Jersey Medical School Institutional Animal Care and Use Committee and conformed to National Research Council guidelines as specified in the *Guide for the Care and Use of Laboratory Animals*. Resected femurs were kept in saline-soaked gauze to prevent dehydration and stored in capped tubes at -20 °C between testing procedures. The μCT and mechanical testing data were obtained at 28 days after fracture. μCT scans were performed using a Bruker SkyScan 1172 (Micro Photonics, Inc., Allentown, PA) with a 0.5 mm aluminum filter and at 70 kVp, 142 mA, frame averaging set at 2, and a voxel size of 17.75 μm. μCT image data were initially reconstructed using the manufacturer's software (NRecon, Bruker, Belgium). Torsional mechanical testing was performed using a servo-hydraulic biaxial mechanical test system (MTS TestStar, Minneapolis, MN) with a 20 Nm torque cell (Interface, Scottsdale, AZ) at 1° per second rotation and data collection rate of 19 Hz. The mechanical testing data were analyzed as described previously (Bergenstock et al., 2005). Femurs were also visually inspected after mechanical testing to determine failure mode (Bergenstock et al., 2005). Mechanical testing failure that occurred as a spiral fracture through the callus was considered a union, failure along the callus fracture site but with some evident callus bridging was considered a partial union, and failure only along the callus fracture site was considered a non-union.

Table 1
Rat mechanical testing values and healing outcomes.

Rat #	Weight (g)	[a]Callus Polar Moment (J_{eff})	Peak Torque (Nmm)	Angle at Failure	Observed Failure Mode
VN10	370	69.46	149	6.28	non-union
VN8	397	72.60	182	14.93	non-union
VN7	396	77.10	193	20.17	non-union
VN91	360	75.82	234	3.92	partial union
VN4	372	89.92	285	8.27	non-union
VN87	394	99.69	312	4.03	partial union
VN2	397	64.35	324	7.79	partial union
VN94	399	65.32	359	12.65	union
VN93	391	65.37	402	9.85	partial union
VN92	384	71.63	445	7.34	union
VN12	391	146.28	469	7.46	partial union
VN88	382	107.14	508	15.65	union

[a] Calculated from μCT images as described (Morgan et al., 2009).

2.2. μCT image data analysis programs

The following MATLAB scripts were developed for this study.

(1) **BoneRotate.m** calculates the intramedullary canal centroid in multiple, user-chosen reconstructed, grayscale μCT images and aligns the reconstructed μCT image set using the centroids to define the neutral *Z*-axis as a best-fit line.
(2) **CreateSlices.m** creates a new series of true cross-sections that are perpendicular to the neutral axis using the reconstructed image data from BoneRotate.m.
(3) **FindPercentFill.m** determines Z-ray lengths and percentage of each Z-ray length filled with positive voxels over the length of the volume of interest.
(4) **PercentInRegion.m** determines Z-ray percent filled over a defined region of interest.
(5) **getZRAY** calculates fracture callus Z-rays and outputs Z-ray lengths in a table and as a heatmap.
(6) **getVox** automates thresholding of μCT images to binary images based on image grayscale values.
(7) **getLink** calculates voxel linkage values (**LVs**) and converts binary images into a 3D linkage matrix.
(8) **segBone** segments 3D linkage matrices based on voxel linkage values (**LVs**) into total, cortical, and fracture callus volumes (**LBV**) and areas (**LBA**).

(9) **getLinkHist** tabulates linkage value frequencies and calculates tissue area (**TA**) and linked bone area (**LBA**) from linked bone volume (**LBV)** objects.
(10) **getRUST** calculates an eRUST score for the femur fracture based on mRUST criteria (Whelan et al., 2010; Litrenta et al., 2015).

In addition, the following previously available MATLAB scripts were used in this study.

(11) **regionprops3** determines and characterizes the number of unconnected objects within a volume of interest (Yeh, 2022).
(12) **Ellipse Fit (Direct Method)** determines the coefficients of an ellipse from a 2D image set of points (Chernov, 2009).
(13) **Calc_J_and_J_eff.m** determines bone or fracture callus polar moment from μCT image data (Morgan et al., 2009).

2.3. Z-ray analysis

The μCT image data for each femur were reoriented using **BoneRotate.m** so that the neutral axis of the healing femur corresponded with the Cartesian Z-axis. Using the reoriented μCT data, a new set of cross-sectional 2D images was generated for each sample using **CreateSlices.m** from which each image corresponded to the X-Y plane perpendicular to the femur neutral, or Z-axis. The new cross-sectional 2D images were used for all subsequent analyses.

After grayscale thresholding, the number, proportion, and longest contiguous length of voxels above the threshold were determined for each Z-ray using **PercentFill**, **PercentInRegion**, and **getZray** as described in the Supplemental Methods. Here, a Z-ray is defined as all the voxels at the same X, Y coordinate within the Z-stack of 2D images which are parallel to the neutral or Z-axis of the femur.

2.4. Image filtering with getVox

Following neutral axis orientation with BoneRotate.m, reconstructed μCT images spanning the break site in each sample were used for the analysis and included 112 image slices representing ~2 mm of the bone at the fracture site. Using **getVox**, the largest grayscale value (LGSV) from all sample images to be analyzed was determined and any voxel greater than or equal to 25 % of the LGSV ($LGSV_{25\%}$) was considered bone. The $LGSV_{25\%}$ threshold gave the most consistent results and provided the best image clarity when assessed visually (Fig. 1).

2.5. Generation of linkage matrices with getLink

The **getLink** script calculated a linkage value (**LV**) for each $LGSV_{25\%}$ positive voxel within the ordered set of binary images from each sample as described in the Supplemental Methods. Using a 3x3x3 matrix of neighboring voxels with the target voxel at the center, each $LGSV_{25\%}$ positive target voxel was assigned a linkage value (**LV**) of 1–27 equivalent to the number of positive voxels within the 3x3x3 matrix. Following this procedure, 3D matrices based on voxel LVs showed that voxels with the highest LVs were localized in cortical bone as compared to the fracture callus (Fig. 2A).

The frequency of voxel LVs within the samples were plotted and a common distribution was found (Fig. 2B and C). Frequency peaks at the absolute maximum LV of 27 and at approximately 19 were noted and theorized to correspond with cortical bone and callus woven bone, respectively.

2.6. Fracture callus segmentation

The cortical bone and external fracture callus in each sample were segmented using LVs and **segBone** script; see the Supplemental Methods for a detailed description of procedures.

Projections of LV in the Z direction were utilized to outline cortical bone (Fig. 3). From this procedure, Cortical Area (CA), and cortical volume (CV) were defined within the Tissue Area (TA), and Tissue Volume (TV). The External Callus Volume (FV) was determined by subtracting the CV from TV. As such, Total Bone Volume (TBV, Cortical Bone Volume (CBV), and External Callus Bone Volume (FBV) were defined. The different volumes were analyzed to determine which spanned the fracture callus and thus define the **Effective Fracture Callus Bone Volume** (**eFBV**), **Effective Cortical Bone Volume** (**eCBV**), and **Effective Total Bone Volume** (**eTBV**). **segBone** saved the volume and list of voxel coordinates for each 3D object found within the TBV, CBV, FBV, eTBV, eCBV, and eFBV along with their respective LV matrices.

2.7. Area and volume determinations

Tissue Area (**TA**) and **Linked Bone Area** (**LBA**) were calculated for the LV matrices generated by **segBone** as described in the Supplemental Methods section. The maximum TA ($\mathbf{TA_{max}}$) and minimum TA ($\mathbf{TA_{min}}$) were identified from among all the 2D images for a given sample and an average TA ($\mathbf{TA_{avg}}$) was calculated for each sample. **getLinkHist** was used to determine **Linked Bone Area** (**LBA**) by summing all voxels (pixels) within the TA of a sample 2D image that had a LV equal to or less than a designated LV threshold. Maximum and minimum LBAs were identified from the sample 2D images and average LBA was calculated from all 2D images of the sample.

Linked Bone Volumes (**LBV**) were calculated for all possible permutations by summing $\mathbf{LBA_{1\text{-}x}}$ from all images within a sample and for which $\mathbf{LBV_{1–27}}$ is equivalent to **Total Bone Volume** (**TBV**). Using this

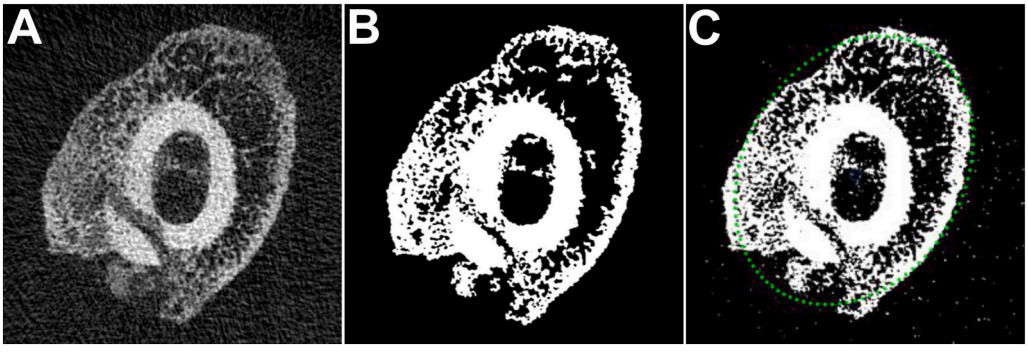

Fig. 1. Image Thresholding and Perimeter Detection. (A) Shown in the left panel is a reconstructed, re-oriented, and cross-sectional grayscale image of a healing rat femur fracture callus. (B) Shown in the middle panel is the binary image produced using the 25 % of the largest grayscale value ($LGSV_{25\%}$) threshold. The $LGSV_{25\%}$ threshold binarization was applied to all μCT images used in this study, unless otherwise noted. (C) Callus perimeter indicated by the green dots was determined using Ellipse Fit (Direct Method) as shown in right panel.

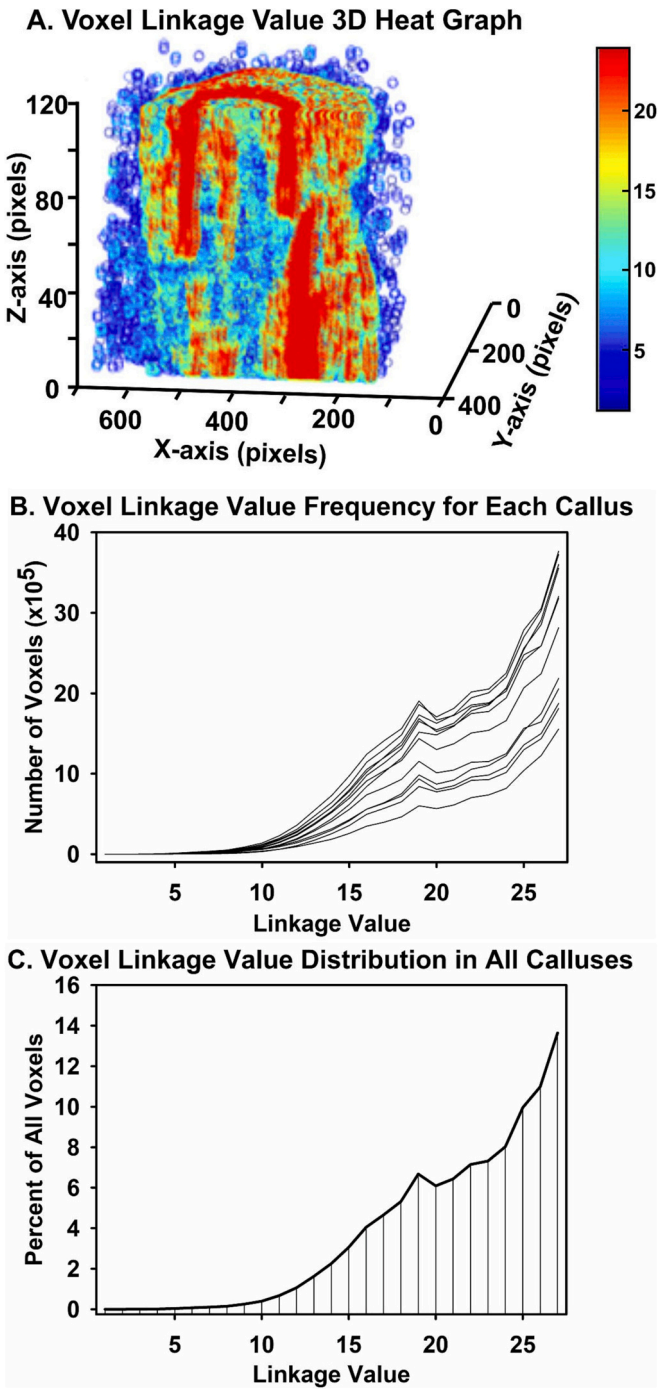

Fig. 2. Fracture Callus Linkage Matrix. The getLink and getVox scripts were used to generate 2D images and 3D volume renderings based on voxel linkage values (LVs). (A) Shown is a longitudinal cut through a 3D linkage volume of a rat femur fracture callus. Each voxel is represented as a pseudo-colored circle in which high LV voxels are colored red and low LV voxels are colored blue. (B) Shown is the frequency distribution of voxel LVs from each rat femur fracture callus. (C) Shown is the percent frequency distribution of voxel LVs from all rat femur fracture calluses examined. Note the consistent peak frequency of voxels at values of 19 (putative callus woven bone) and 27 (putative cortical bone).

approach, different LV thresholds could be used to compare distributions of connectivity between samples.

2.8. Automated mRUST (eRUST) scoring methodology

Individual objects within the eCBV and eFBV were computationally compared to automate a fracture union status calculation, termed eRUST, as described in the Supplemental Methods and based on the established mRUST radiograph scoring method (Table 2) (Litrenta et al., 2015).

2.9. Statistics

Only the mechanical testing peak torque values were correlated with the different μCT outcome measures as peak torque is empirically the most direct measure of callus mechanical integrity when performing destructive, torsional testing. The data were compared using Pearson's R^2 generated from MATLAB regression functions. Intraclass correlations coefficients (ICC) were calculated with STATA version MP2 15 (College Station, Texas).

3. Results

3.1. Z-ray analysis

Multiple methods were used to compare femur mechanical testing values to different Z-ray calculations. The two most successful approaches involved using volumes of interest that began approximately 1 mm proximal and stopped 1 mm distal of the fracture site.

In one approach, the volume of interest was further defined as the outer portion of the fracture callus from 100 % of the callus periphery to 75 % of the callus periphery as determined by edge detection of the fracture callus in Z-axis projection. The proportion of the highest filled Z-rays in the callus periphery volume of interest positively correlated with callus peak torque ($R^2 = 0.63$).

In another approach, the longest contiguous length of positive voxels after grayscale thresholding within each Z-ray was determined and analyzed as frequencies of Z-rays within percent intervals of the defined callus region of interest length (Fig. 4). Continuous Z-ray lengths were grouped in 10 % increments of the overall region of interest length. The number of Z-rays that were $\geq$ 90 % of the callus region of interest length ($Z_{90}N$) showed the highest correlation to sample peak torque values ($R^2 = 0.79$; Fig. 5).

3.2. Segmentation of cortical bone and external fracture callus

The **segBone** approach produced an unbiased and repeatable method for segmenting bone. Using LVs, the boundary between the femur cortical bone and external fracture callus bone was easily identified (Fig. 6). This enabled segmentation of the cortical bone from the external fracture callus so that total, cortical, and callus linked bone areas (**LBA**) and linked bone volumes (**LBV**) could be calculated.

3.3. Correlating μCT linkage analysis parameters to peak torque

A correlation analysis was performed using each sample peak torque value and each $LBA_{1\text{-}x}$ value for each μCT image of that sample within the volume of interest. The specimen image LBAs analyzed included the maximum LBA (LBA_{max}), the minimum LBA (LBA_{min}), and the mean from all μCT images in the sample volume of interest (LBA_{avg}). The LBA values were normalized to TA_{max}, TA_{min}, and TA_{avg} for those sample images within the volume of interest. While many of the calculated values showed strong correlations to the mechanical testing data, the highest R^2 values were calculated at a linkage value of 13 ($LBA_{1–13}$). R^2 tended to reach a maximum at linkage values between 13 and 19 (Fig. 7A). R^2 values were lower for $LBA_{1–27}$ (TBA). Of 12 calculations analyzed, LBA_{min} and LBA_{min}/TA_{max} had the highest correlations to callus peak torque values (Fig. 7B and C). LBA_{min} had a better correlation at a connection value of 13 than at 27 (R^2 = 0.735 vs 0.669 respectively). For LBA_{min}/TA_{max}, the correlation was better for $LBA_{min\ (1–13)}$ than for $LBA_{min(1–27)}$ (R^2 = 0.764 vs 0.689 respectively; Table 3). Similar trends were found for all measures suggesting that the less dense,

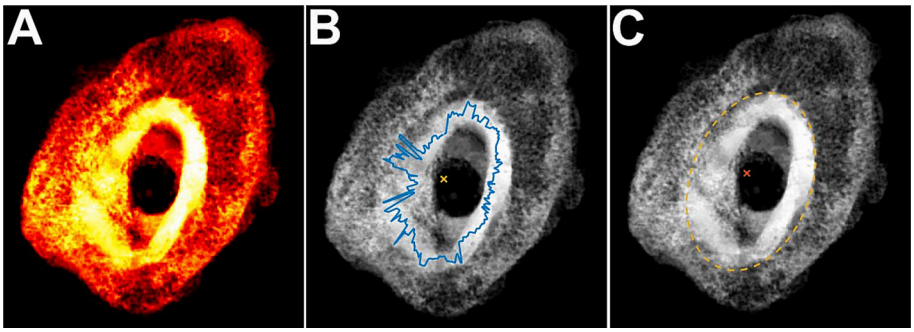

Fig. 3. Two-dimensional visualization of callus structure. Shown are 2D compressed images of a fracture callus VOI as (A) a heat map of the normalized *Z*-ray LVs in a callus, (B) the callus centroid (yellow X) and outline (blue) of highest normalized Z-ray LV encountered circumferentially from the centroid, and (C) the callus centroid (red X) and a best-fit ellipse based on the circumferential Z-rays with highest normalized LVs.

Table 2
A comparison of mRUST and getRUST Scoring Criteria.

Quadrant Score	mRUST Criteria		getRUST Criteria			
			Does volume spans > 85 % callus length			
	Fracture Line	Callus	CBV		FBV	
			$LV_{1–27}$	$LV_{26–27}$	$LV_{1–27}$	$LV_{26–27}$
4	Invisible	Remodeling	Yes	Yes	Yes	Yes
3	Visible	Bridging	Yes	No	Yes	No
2	Visible	Present	No	No	Yes	No
1	Visible	Absent	No	No	No	No

trabecular bone volume correlates better to the mechanical properties of the fracture callus at this point during healing. Of the 12 calculated values, six had correlation coefficients above 0.5 when compared to callus peak torque values (Table 3). Using a linkage value of 13 improved the correlation to callus peak torque values by approximately 5.2 ± 1.5 %.

3.4. Automated mRUST Scoring Calculations (eRUST)

Segmentation of the fracture callus using LVs enabled development of the getRUST script to assess fracture healing from the μCT image data using an unbiased, computational approach. Using getRUST, eRUST scores were calculated for each of the rat femur fracture calluses. In addition, 3 trained raters used the modified RUST (mRUST) scoring system to rate the 12 rat femur fracture calluses using both anterior-posterior and medial-lateral digital radiographs.

An intraclass correlation coefficient (ICC) was calculated for the mRUST scores from the 3 raters and the eRUST scores calculated by the getRUST script (12 ratings by 4 raters). The ICC value for the rater mRUST and getRUST measurements was 0.88 indicating strong correlations between computed algorithm scoring of the μCT image data and scoring performed by individuals.

The mRUST scores from the 3 trained raters had a mean of 10.08, standard deviation of 4.05, and an R^2 value of 0.745 when correlated to fracture callus peak torque values (Table 4). In contrast, the eRUST scores calculated using the getRUST script from the same 12 femur fracture calluses had a mean of 11.42, standard deviation of 3.73, and an R2 value of 0.863 when correlated to callus peak torque values (Table 4).

4. Discussion

Here we describe novel approaches for translating μCT image data to estimate a fracture callus structural property. For both the *Z*-ray analysis and the calculated mRUST scoring (eRUST), the correlation between the two novel μCT image data measures of healing and callus peak torque were $R^2 = 0.79$ for the Zn90 Z-ray analysis and $R^2 = 0.863$ for the eRUST scoring. Other approaches to correlate callus dimensions measured using voxel linkage values to callus peak torque values found that the minimum linked bone area (LBA_{min}) or LBA_{min} normalized to maximum tissue area (LBA_{min}/TA_{max}) produced correlations with R^2 values of 0.736 and 0.764, respectively. One prior study found associations between peak torque and BV or BV/TV with Pearson's correlation

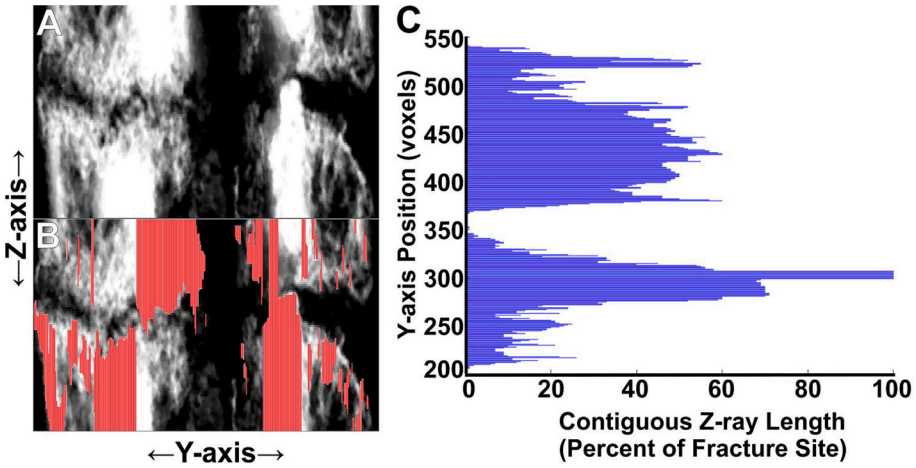

Fig. 4. Mapping Contiguous Z-rays at the Fracture Site. Panel A shows approximately 40 X-axis grayscale images of a rat femur fracture callus stacked as a compressed 2D image. The femur intramedullary canal and fracture lines are evident. Panel B shows where the longest, contiguous Z-rays (red) from one X-axis grayscale image mapped on the compressed 2D image. Panel C shows the relative length of the contiguous Z-rays as mapped along the Y-axis.

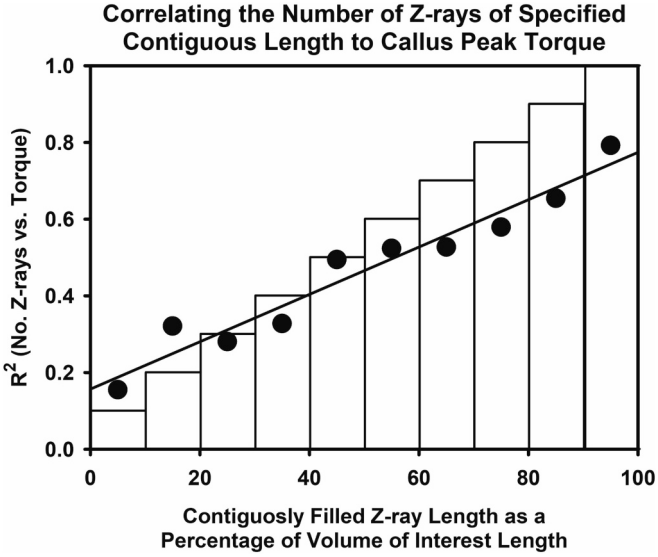

Fig. 5. Correlating Contiguous Z-ray Length to Callus Peak Torque. The longest contiguous length of positive voxels was determined for each Z-ray and normalized as a percentage of maximum Z-ray length. The number of Z-rays with the longest, contiguous length of positive voxels were summed for each decile of maximum Z-ray length and then correlated to the corresponding callus peak torque. The graph shows the R^2 values from frequencies of Z-rays within each decile for all calluses. The highest R^2 value was obtained when the summed number of longest, contiguous Z-rays >90 % of maximum Z-ray length (Zn90) was correlated to peak torque.

coefficients of 0.8 and 0.7, respectively, which would be equivalent to R^2 values of 0.64 and 0.49 (Fiset et al., 2018). Willems et al. (2022) performed a systematic review comparing CT-assessed microarchitecture parameters to mechanical and histologic signs of healing (Willems et al., 2022). As reported by Willems et al., 3 of 6 studies found no or weak associations ($R^2 < 0.4$) between BV and mechanical outcomes, while 3 studies reported moderate ($R^2 = 0.4–0.7$) or strong ($R^2 > 0.7$) associations between BV and mechanical outcomes. BV/TV was assessed relative to mechanical outcomes in 4 studies of which only 1 reported a moderate association. In contrast, 2 studies found moderate associations ($R^2 = 0.5$) and 1 study found a strong association ($R^2 = 0.8$) between torsional rigidity (GJ) calculated from μCT image data using estimates of specimen shear modulus (G) based on voxel radiodensities and polar moment (J) based on cross-sectional bone areas as compared to empirically determined torsional rigidity (Shefelbine et al., 2005; Nazarian et al., 2010; Wright et al., 2012; Willems et al., 2022). Many prior studies focused on the amount of bone formed in the callus as BV or BV/TV. However, the amount of bone formed does not necessarily equate to bone bridging the fracture gap. The current methods, instead, focused on the amount of bone bridging the fracture as the number of contiguously filled *Z*-rays ($Z_{90}N$), the minimum amount of cross-sectional bone area in the callus volume (LBA_{min}/TA_{max}), or the number and quality of connected bone fragments spanning the fracture site (eRUST) and appear to produce better correlations with callus mechanical integrity. The current and past results show the heterogeneity of approaches and outcomes when attempting to estimate bone mechanical properties from μCT image data.

A significant advantage of the current approaches is the relative simplicity of the calculations defined in the various MATLAB scripts. Voxel linkage values can be easily calculated and used to calculate linked bone area, bone volume measurements, and computed eRUST scoring. In all cases, the analyses are conducted without subjective input from human evaluators and provide objective and quantitative estimates of specimen peak torque. Modeling approaches, such as finite element modeling, may yield better correlations between the μCT image data and any mechanical measure of the callus (Shefelbine et al., 2005). However, such approaches are more computationally intensive and potentially biased by the model employed.

4.1. *Z-ray analysis*

The Z-ray analysis seeks to determine how well a particular bone fragment is connected to other fragments and appears to be an intuitive measure of fracture healing. Our analysis, however, found that use of *Z*-rays required additional optimization. When analyzing *Z*-rays based upon the percentage of *Z*-ray length filled with positive voxels, the *Z*-rays associated with the cortical bone have a high percentage of positive voxels (see Fig. 3A) yet failed to correlate well with callus peak torque (Subramanian, 2015). Better correlations with callus peak torque were

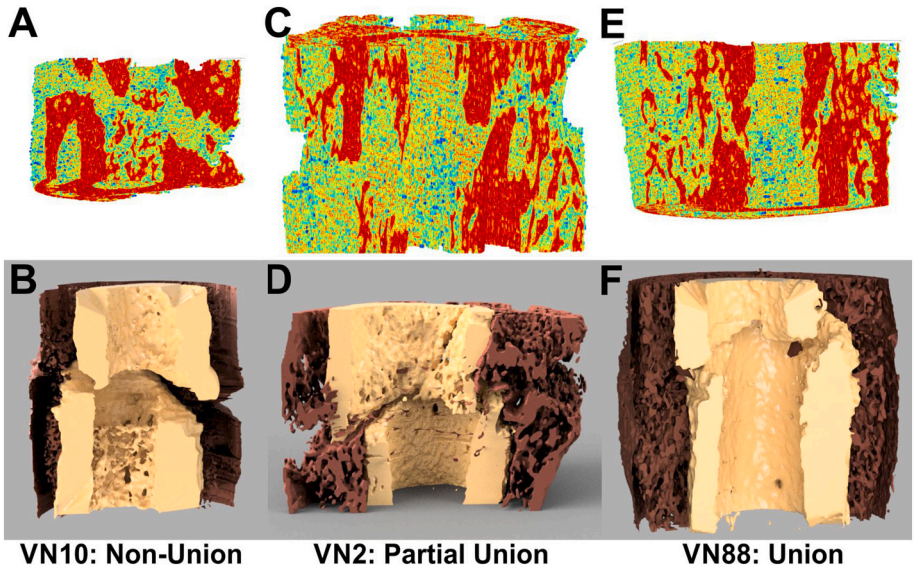

Fig. 6. Three-Dimensional Visualization of Callus Structure using Voxel Linkage Values. Shown are 3D renderings of a fracture callus non-union (A, B), incomplete union (C, D), and union (E, F) depicting linkage value distributions (red = highest LVs) for each callus (A, C, E) and following segmentation into external callus (brown) and cortical bone (tan; B, D, F). The 3D renderings shown in panels B, D, and F were rendered in Fusion 360 (Autodesk, San Francisco, CA) after processing the linkage value data with InVesalius (available via Github) and Meshmixer (Autodesk).

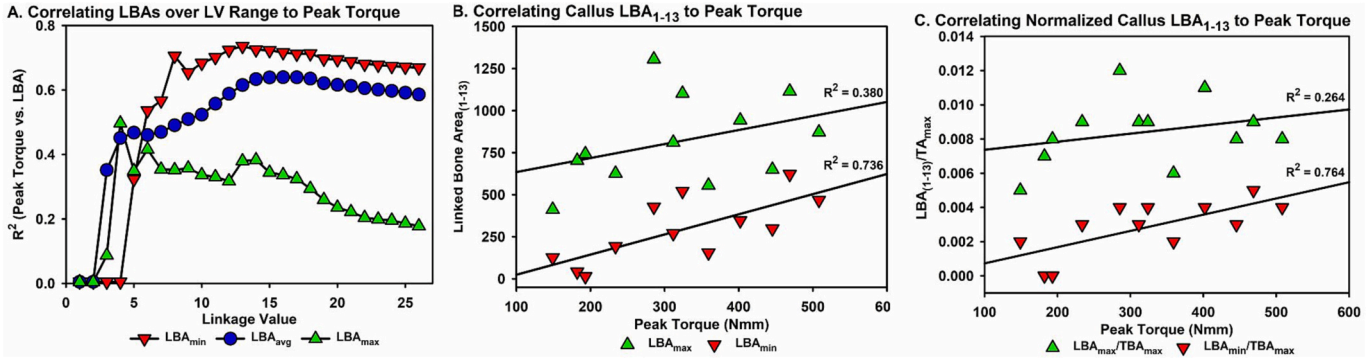

Fig. 7. Correlating Linked Bone Area to Callus Peak Torque. (A) Callus minimum, maximum, and average LBA at each LV were correlated to each callus peak torque level and the resulting mean R^2 value for all 12 calluses tested are shown. The highest R^2 value was obtained using a LV of 13 and the minimum LBA. (B) Shown is a direct comparison of minimum and maximum $LBA_{1–13}$ with callus peak torque, demonstrating a higher R^2 for LBA_{min}. (C) Shown is a direct comparison of callus peak torque to minimum and maximum $LBA_{1–13}$ normalized to maximum TA, demonstrating a higher R^2 for normalized minimum $LBA_{1–13}$.

Table 3
Coefficients of Determination (R^2) between Sample Peak Torque Values and Linked Bone Area (LBA) Values.

	R^2 values for:			
	Non-normalized LBA:	LBA Normalized to:		
		TA_{min}	TA_{max}	TA_{avg}
LBA_{min}	0.736	0.570	0.764	0.697
LBA_{max}	0.380	−0.120	0.264	0.037
LBA_{avg}	0.615	0.198	0.603	0.430

Table 4
Comparison of mRUST Scoring to calculated getRUST Scoring.

Rat	Peak Torque (Nmm)	getRUST	Avg. Rater	Rater 1	Rater 2	Rater 3
		eRUST	mRUST	mRUST	mRUST	mRUST
VN10	149	5	10	10	10	10
VN8	182	7	6.7	4	6	10
VN7	193	7	5.3	4	4	8
VN91	234	13	8.7	6	7	13
VN4	285	9	5.3	4	4	8
VN87	312	13	11.7	12	9	14
VN2	324	11	8.7	9	7	10
VN94	359	14	11.7	11	8	16
VN93	402	11	8	9	5	10
VN92	445	16	15.7	16	15	16
VN12	469	16	14	14	12	16
VN88	508	15	15.3	15	15	16
Mean	322	11.4	10.1	9.5	8.5	12.2
SD	119	3.73	3.62	4.32	3.85	3.25
SD (%)	37 %	33 %	36 %	45 %	45 %	27 %
R^2	1	0.863	0.743	0.778	0.635	0.705

obtained when the volume of interest was limited to the callus periphery ($R^2 = 0.63$) (Subramanian, 2015). Typical callus structures at 4 weeks after fracture (Fig. 6) support these correlations since bone bridging is primarily apparent in the external callus while the fracture is still evident in the cortical bone. In contrast, the number of *Z*-rays that were contiguously filled with positive voxels at a length greater than or equal to 90 % of Z-ray length (Zn90) for the volume of interest correlated better with callus peak torque ($R^2 = 0.79$). This later approach of using contiguously filled Z-ray length (Zn90) has additional advantages. The Zn90 approach does not require additional calculations to determine external callus periphery or cortical bone area. Rather, the Zn90 approach only requires re-orienting the bone in the neutral axis, defining the proximal and distal limits of the volume to be analyzed, applying any necessary thresholding, and then counting the number of Z-rays contiguously filled at 90 % or more. The Zn90 approach also does not require a priori assumptions of callus structure. Thus, the Zn90 approach may be best for assessing later stages of healing as the cortical bone reforms and fracture lines are resolved. Additional experiments using time points prior to callus bridging of the fracture, during bridging, and during remodeling may better define the utility of the Zn90 approach.

We did not attempt to optimize Z-ray length as defined by the volume of interest. The analyses performed in this work used a 2 mm Z-ray length. We suspect that similar to voxel thresholding, maximum Z-ray length may also be an important factor. If maximum Z-ray length is too short, then proportionally more contiguous Z-rays would be available to correlate with specimen mechanical properties. Conversely, if maximum Z-ray length is too long, proportionally fewer contiguous Z-rays would be available to correlate with specimen mechanical properties. Clinically and experimentally, comminuted, oblique, or otherwise non-transverse fractures of the long bones would necessitate altering the volume of interest, which could affect Z-ray analysis outcomes.

4.2. Linkage values

Linkage values (LVs) provide a novel descriptive dimension to each voxel that cannot be provided by grayscale or Hounsfield unit scaling. One unexpected finding was how well LVs could be used to distinguish cortical bone from callus woven bone. For the experiments reported here, image data were initially grayscale thresholded ($LGSV_{25\%}$) to binarize voxels which produced what appeared to be an accurate representation of bony voxels within each μCT image. The $LGSV_{25\%}$ may have been a fortuitous choice since conceivably, a lower threshold would have increased LVs in callus volume voxels without affecting LVs in the cortical volume voxels, thus complicating the distinction between external callus and cortical bone. Conversely, a higher threshold may have eliminated portions of the callus from the analysis that were germane to predicting callus peak torque values. Therefore, one aspect of this study that warrants further investigation is whether LVs can be optimized by altering thresholding methods or methods for calculating the LVs. Alternative approaches to thresholding image data prior to generating LVs could potentially improve estimations of mechanical strength or segmentation in different tissue types. As an example, grayscale images could be standardized to known radiodensity standards or to Hounsfield units to better define upper and lower limits for tissue radiodensity thresholding. When subsequently analyzed using getLink, only tissues of similar radiodensity would be expected to have high LVs. Thus, by slightly altering the getVox procedure, getLink and segBone (or a similar segmentation programs) potentially could be used to segment and measure specific tissues as well.

The distribution of voxel LVs observed in study samples coincided with peaks at 19 and 27. The bimodal distribution of LV frequencies

appears to be consistent with external fracture callus voxels having lower LVs and cortical bone having higher LVs. This is consistent with the lower expected density of newly formed bone in the surrounding fracture callus compared to the dense, compact bone in the spared cortical areas. Studying changes in LV distributions throughout the healing process could be useful for empirically assessing fracture healing progression. Assuming $LV_{1–27}$ does not change, then one could expect that the lesser LV peak to progressively increase from $LV_{1–19}$ (or possibly less at earlier times) to $LV_{1–27}$ as healing proceeds.

4.3. Linkage areas

Defining the area and volume of interest both by size and thresholding appear to be critical factors when attempting to relate μCT imaging data to specimen mechanical properties.

Correlating the minimum Linked Bone Area (LBA_{min}) to callus peak torque produced a good R^2 value (0.736) and was not dependent on a callus volume measure. Normalizing LBA_{min} to callus maximum tissue area (LBA_{min}/TA_{max}) produced a slightly better coefficient of determination ($R^2 = 0.764$). These measurements required re-orienting the femoral canal into the neutral axis and thresholding the images at $LGSV_{25\%}$. Bone area was measured for each image by summing the number of positive voxels in that image. For some applications, using LBA_{min} or LBA_{min}/TA_{max} may be sufficient for estimating callus mechanical properties.

Interestingly LBA_{min} derived from $LV_{1–13}$ correlated best with mechanical testing values. This suggests that the $LV_{1–13}$ represents trabecular bone and that the amount of trabecular bone correlates most strongly with callus peak torque at the 4-week timepoint. Conversely, the high correlation between peak torque and LBA_{min} from $LV_{1–13}$ indicates that, at least at the 4-week time point, cortical bone contributes little to sample peak torque. More data needs to be collected from healing fractures at different times after fracture and from different bone fractures to better evaluate the use of LVs for assessing the healing process.

4.3.1. eRUST

Of the μCT data analysis methods attempted, the computationally derived eRUST score provided the highest correlation to callus peak torque levels ($R^2 = 0.863$). Similar to the *Z*-ray analysis, bone volumes identified during the eRUST procedure would also be subject to variability associated with thresholding and volume of interest settings. Further, eRUST relies upon a set scoring system from 4 to 16 for any one callus rather than a continuous variable. Thus, a non-parametric eRUST score is compared to a continuous outcome value for peak torque. This could potentially limit correlation of an eRUST score to a peak torque range which may be inadequate for some experimental purposes but could be acceptable as a clinical evaluation tool.

Segmenting cortical bone (Cortical Object) from the external callus (Callus Object) was difficult to model due to asymmetry in callus formation. For the rat femur, an ellipse was the most effective geometry for modeling the cortical portion of the femur diaphysis. However, the best-fit ellipse did not perfectly match every sample (Chernov, 2009). For these reasons, the calculated best-fit ellipse was undersized by 30 % to avoid including any external callus with the cortical bone. Otherwise, the extra volume from a larger ellipse may have erroneously reduced the calculated Callus Object volume and integrity of the external callus. Use of the 30 % reduced ellipse model ensured that the external callus was not incorporated into the determination of bony union between the cortical bone segments. As with LVs, alteration of image segmentation procedures using getLink and segBone would change object volumes and identification and could modify eRUST scores.

There is currently no universally accepted clinical standard for assessing progress in fracture healing. In practice, fracture healing assessments are done using radiographic imaging, clinical assessments, and patient-reported outcomes, which have low inter-observer and intra-observer reliability. Cooke et al. found that when 7 surgeons examined 15 sets of plain radiographs of scaphoid non-unions, their RUST or mRUST assessments were not consistent or reproducible ($\kappa = 0.46–0.54$) (Cooke et al., 2018). Though the mRUST scoring system was found to increase inter-observer agreement ($\kappa = 0.86$), mRUST scores were only weakly correlated to locomotory function ($r = 0.046$) (Whelan et al., 2010; Field and Ruthenbeck, 2018). μCT scan evaluations for tibial non-union have shown 100 % sensitivity but several false positives lowered specificity to 62 % (Bhattacharyya et al., 2006). Based on the current study, eRUST scoring, which is based on the mRUST scoring system, produces an objective assessment of fracture healing with greater correlation to mechanical testing data than investigators using the traditional mRUST scoring system. Because eRUST uses linkage values, which are calculated from microarchitectural measurements of μCT image data that are not visible to an evaluator, eRUST may also provide a lower false positive rate. However, the false positive rate has not yet been tested.

Both observer scoring of 2D callus images and eRUST scoring produced positive correlations to fracture callus peak torque values, though eRUST yielded a better correlation. The high intraclass correlation (ICC = 0.88) indicated that eRUST scoring of each sample was very similar to that of the individual raters However, observers are limited by visually interpreting 2D images as 3D objects, whereas the eRUST procedure analyzes the μCT imaging data in 3D. The results suggest that the eRUST scoring could have useful experimental and clinical applications because the eRUST computation applies a standardized scoring system that eliminates both observer bias and the need for multiple evaluators to score the same dataset to account for that bias.

4.4. Study limitations and future directions

Fracture callus size, morphology, and tissue composition change as healing progresses. Any indirect measure of fracture healing that could identify potential indications of delayed healing or non-union formation would be a highly useful tool. In this study, we only assessed healing at 4 weeks after fracture. This timepoint was chosen because in previous experiments, we found that callus bridging was evident in some, but not all, experimental rats at this time (Simon et al., 2002; Cottrell and O'Connor, 2009). Thus, the 4-week timepoint would yield bridged, partially bridged, and unbridged calluses. An endpoint assessment as employed here is useful for determining healing status, but analysis of serial μCT image data sets could determine if healing is progressing, is sufficiently complete, or has stopped progressing. Further analyses of such serial μCT image data sets may identify telltale signs of impaired healing that could trigger pre-emptive treatment.

A significant limitation of using serial CT examination to measure fracture healing progress is the radiation dose from multiple X-ray exposures during each CT scan. Clinically, most simple fractures are diagnosed and treated using 2D X-rays and fluoroscopy. CT is more likely to be used for complex fractures to develop plans for fracture reduction. For research animal models of fracture healing, more latitude is available for serial CT assessments, though radiation dose effects are still a critical consideration. Thus, radiation exposure from current CT or μCT imaging technology will likely limit serial CT and μCT assessments.

The only mechanical parameter to which the μCT image data were correlated was peak torque, which is a structural property of the callus and the mechanical testing value that was directly measured from each callus. This is a limitation of the study. However, we would not necessarily expect Zn90, LBAmin/TAmax, or eRUST values that were optimized to correlate with peak torque to also correlate with other callus mechanical properties such as rigidity, modulus or toughness. As each mechanical property describes a certain aspect of the callus, so to we would expect that additional methods for analyzing CT image data can be devised that would correlate with other mechanical properties. Additional experiments and analyses are planned to correlate μCT image data to empirical structural and material mechanical properties of

fracture callus collected at different times after fracture as well as from intact bone. These future experiments are expected to provide a more complete evaluation of the utility of using *Z*-ray analysis, linked bone measures, eRUST scoring, or other novel methods as indirect measure of callus or bone mechanical properties. Similarly, situations involving complex long bone fractures, non-long bone fractures, segmental defects, or bone fusions will require modifications of the above μCT image data analysis procedures to produce useful estimates of healing progression.

CRediT authorship contribution statement

Yazan Kadkoy: Writing – review & editing, Validation, Software, Methodology, Investigation, Formal analysis. **Sangeeta Abraham:** Writing – review & editing, Software, Methodology, Investigation, Formal analysis. **Peter Michael:** Software, Methodology. **Tasmima Tazin:** Writing – original draft. **Charlene Wetterstrand:** Writing – review & editing, Formal analysis. **J. Patrick O'Connor:** Writing – review & editing, Writing – original draft, Methodology, Funding acquisition, Conceptualization.

Declaration of competing interest

None.

Data availability

The MATLAB scripts developed in this manuscript are available as a MATLAB application (LinkAN.mlapp) available on GitHub at https://github.com/YazKad/LinkAn.git.

Acknowledgments

This work was supported by the National Institute of Arthritis and Musculoskeletal and Skin Diseases of the National Institutes of Health under Award Number R01AR069044, the Rutgers-New Jersey Medical School Department of Orthopaedics, the Fred F. Buechel, M.D., Chair for Joint Replacement at New Jersey Medical School, and the Fred F. Behrens, M.D. Endowed Chair in Orthopedic Trauma Education. All MATLAB scripts discussed in this manuscript as well as a compiled GUI are publicly available on GitHub at: https://github.com/YazKad/LinkAn.git.

Appendix A. Supplementary data

Supplementary data to this article can be found online at https://doi.org/10.1016/j.bonr.2023.101726.

References

Anani, T., Castillo, A.B., 2022. Mechanically-regulated bone repair. Bone 154, 116223. https://doi.org/10.1016/j.bone.2021.116223.

Augat, P., Merk, J., Ignatius, A., Margevicius, K., Bauer, G., Rosenbaum, D., Claes, L., 1996. Early, full weightbearing with flexible fixation delays fracture healing. Clin. Orthop. Relat. Res. 328, 194–202. https://doi.org/10.1097/00003086-199607000-00031.

Bergenstock, M., Min, W., Simon, A.M., Sabatino, C., O'Connor, J.P., 2005. A comparison between the effects of acetaminophen and celecoxib on bone fracture healing in rats. J. Orthop. Trauma 19 (10), 717–723. https://doi.org/10.1097/01.bot.0000184144.98071.5d.

Bhattacharyya, T., Bouchard, K.A., Phadke, A., Meigs, J.B., Kassarjian, A., Salamipour, H., 2006. The accuracy of computed tomography for the diagnosis of tibial nonunion. J. Bone Joint Surg. Am. 88 (4), 692–697. https://doi.org/10.2106/JBJS.E.00232.

Bouxsein, M.L., Boyd, S.K., Christiansen, B.A., Guldberg, R.E., Jepsen, K.J., Muller, R., 2010. Guidelines for assessment of bone microstructure in rodents using micro-computed tomography. J. Bone Miner. Res. 25 (7), 1468–1486. https://doi.org/10.1002/jbmr.141.

Chernov, N., 2009. Ellipse Fit (Direct Method). https://www.mathworks.com/matlabcentral/fileexchange/22684-ellipse-fit-direct-method.

Cooke, M.E., Hussein, A.I., Lybrand, K.E., Wulff, A., Simmons, E., Choi, J.H., Litrenta, J., Ricci, W.M., Nascone, J.W., O'Toole, R.V., Morgan, E.F., Gerstenfeld, L.C., Tornetta 3rd, P., 2018. Correlation between RUST assessments of fracture healing to structural and biomechanical properties. J. Orthop. Res. 36 (3), 945–953. https://doi.org/10.1002/jor.23710.

Cottrell, J.A., O'Connor, J.P., 2009. Pharmacological inhibition of 5-lipoxygenase accelerates and enhances fracture-healing. J. Bone Joint Surg. Am. 91 (11), 2653–2665. https://doi.org/10.2106/JBJS.H.01844.

Cunningham, B.P., Brazina, S., Morshed, S., Miclau 3rd, T., 2017. Fracture healing: a review of clinical, imaging and laboratory diagnostic options. Injury 48 (Suppl. 1), S69–s75. https://doi.org/10.1016/j.injury.2017.04.020.

Field, J.R., Ruthenbeck, G.R., 2018. Qualitative and quantitative radiological measures of fracture healing. Vet. Comp. Orthop. Traumatol. 31 (1), 1–9. https://doi.org/10.3415/vcot-17-03-0042.

Fiset, S., Godbout, C., Crookshank, M.C., Zdero, R., Nauth, A., Schemitsch, E.H., 2018. Experimental validation of the Radiographic Union Score for Tibial fractures (RUST) using micro-computed tomography scanning and biomechanical testing in an in-vivo rat model. J. Bone Joint Surg. Am. 100 (21) https://doi.org/10.2106/Jbjs.18.00035.

Kenwright, J., Richardson, J.B., Goodship, A.E., Evans, M., Kelly, D.J., Spriggins, A.J., Newman, J.H., Burrough, S.J., Harris, J.D., Rowley, D.I., 1986. Effect of controlled axial micromovement on healing of tibial fractures. Lancet 2 (8517), 1185–1187. https://doi.org/10.1016/s0140-6736(86)92196-3.

Litrenta, J., Tornetta 3rd, P., Mehta, S., Jones, C., O'Toole, R.V., Bhandari, M., Kottmeier, S., Ostrum, R., Egol, K., Ricci, W., Schemitsch, E., Horwitz, D., 2015. Determination of radiographic healing: an assessment of consistency using RUST and modified RUST in metadiaphyseal fractures. J. Orthop. Trauma 29 (11), 516–520. https://doi.org/10.1097/bot.0000000000000390.

Morgan, E.F., Mason, Z.D., Chien, K.B., Pfeiffer, A.J., Barnes, G.L., Einhorn, T.A., Gerstenfeld, L.C., 2009. Micro-computed tomography assessment of fracture healing: relationships among callus structure, composition, and mechanical function. Bone 44 (2), 335–344. https://doi.org/10.1016/j.bone.2008.10.039.

Morshed, S., Corrales, L., Genant, H., Miclau 3rd, T., 2008. Outcome assessment in clinical trials of fracture-healing. J. Bone Joint Surg. Am. 90 (Suppl. 1), 62–67. https://doi.org/10.2106/JBJS.G.01556.

Nazarian, A., Pezzella, L., Tseng, A., Baldassarri, S., Zurakowski, D., Evans, C.H., Snyder, B.D., 2010. Application of structural rigidity analysis to assess fidelity of healed fractures in rat femurs with critical defects. Calcif. Tissue Int. 86 (5), 397–403. https://doi.org/10.1007/s00223-010-9353-4.

Nyman, J.S., Munoz, S., Jadhav, S., Mansour, A., Yoshii, T., Mundy, G.R., Gutierrez, G.E., 2009. Quantitative measures of femoral fracture repair in rats derived by micro-computed tomography. J. Biomech. 42 (7), 891–897. https://doi.org/10.1016/j.jbiomech.2009.01.016.

Ruiz, F.K., Fu, M.C., Bohl, D.D., Hustedt, J.W., Baumgaertner, M.R., Leslie, M.P., Grauer, J.N., 2014. Patient compliance with postoperative lower extremity touch-down weight-bearing orders at a level I academic trauma center. Orthopedics 37 (6), e552–e556. https://doi.org/10.3928/01477447-20140528-55.

Shefelbine, S.J., Simon, U., Claes, L., Gold, A., Gabet, Y., Bab, I., Müller, R., Augat, P., 2005. Prediction of fracture callus mechanical properties using micro-CT images and voxel-based finite element analysis. Bone 36 (3), 480–488. https://doi.org/10.1016/j.bone.2004.11.007.

Simon, A.M., Manigrasso, M.B., O'Connor, J.P., 2002. Cyclo-oxygenase 2 function is essential for bone fracture healing. J. Bone Miner. Res. 17 (6), 963–976. https://doi.org/10.1359/jbmr.2002.17.6.963.

Subramanian, S., 2015. Methods to Limit BMP-2 Activity and Improve Bone Healing. Ph. D, Rutgers-New Jersey Medical School.

Turner, C.H., Burr, D.B., 1993. Basic biomechanical measurements of bone: a tutorial. Bone 14 (4), 595–608.

Weis, J.A., Granero-Molto, F., Myers, T.J., Longobardi, L., Spagnoli, A., Miga, M.I., 2012. Comparison of microCT and an inverse finite element approach for biomechanical analysis: results in a mesenchymal stem cell therapeutic system for fracture healing. J. Biomech. 45 (12), 2164–2170. https://doi.org/10.1016/j.jbiomech.2012.05.033.

Whelan, D.B., Bhandari, M., Stephen, D., Kreder, H., McKee, M.D., Zdero, R., Schemitsch, E.H., 2010. Development of the radiographic union score for tibial fractures for the assessment of tibial fracture healing after intramedullary fixation. J. Trauma 68 (3), 629–632. https://doi.org/10.1097/TA.0b013e3181a7c16d.

Willems, A., Içli, C., Waarsing, J.H., Bierma-Zeinstra, S.M.A., Meuffels, D.E., 2022. Bone union assessment with Computed Tomography (CT) and statistical associations with mechanical or histological testing: a systematic review of animal studies. Calcif. Tissue Int. 110 (2), 147–161. https://doi.org/10.1007/s00223-021-00904-6.

Wittauer, M., Burch, M.A., McNally, M., Vandendriessche, T., Clauss, M., Della Rocca, G. J., Giannoudis, P.V., Metsemakers, W.J., Morgenstern, M., 2021. Definition of long-bone nonunion: a scoping review of prospective clinical trials to evaluate current practice. Injury 52 (11), 3200–3205. https://doi.org/10.1016/j.injury.2021.09.008.

Wright, D.A., Nam, D., Whyne, C.M., 2012. A comparison of stereology, structural rigidity and a novel 3D failure surface analysis method in the assessment of torsional strength and stiffness in a mouse tibia fracture model. J. Biomech. 45 (13), 2236–2240. https://doi.org/10.1016/j.jbiomech.2012.06.016.

Yang, J.S., Otero, J., McAndrew, C.M., Ricci, W.M., Gardner, M.J., 2013. Can tibial nonunion be predicted at 3 months after intramedullary nailing? J. Orthop. Trauma 27 (11), 599–603. https://doi.org/10.1097/BOT.0b013e31828f5821.

Yeh, C., 2022. regionsprops3. https://github.com/joe-of-all-trades/regionprops3 (Retrieved August 8, 2022).